

**SEEKING THE LOCAL CONVERGENCE DEPTH. II.
TULLY–FISHER OBSERVATIONS OF THE CLUSTERS A114,
A119, A194, A2295, A2457, A2806, A3193, A3381, AND A3744**

DANIEL A. DALE,^{1,2} RICCARDO GIOVANELLI,^{1,2} MARTHA P. HAYNES,¹ AND
MARCO SCODEGGIO^{1,3}

Center for Radiophysics and Space Research and National Astronomy and Ionosphere
Center, Cornell University, Ithaca, NY 14853

Electronic mail: dale,riccardo,haynes,scodeggi@astrosun.tn.cornell.edu

EDUARDO HARDY²

Department of Physics, Laval University, Ste–Foy, P.Q., G1K 7P4, Canada

Electronic mail: hardy@phy.ulaval.ca

LUIS E. CAMPUSANO²

Observatorio Astronómico Cerro Calán, Departamento de Astronomía, Universidad de
Chile, Casilla 36-D, Santiago, Chile

Electronic mail: lcampusa@das.uchile.cl

ABSTRACT

We present Tully–Fisher (TF) observations for nine rich Abell clusters of galaxies. This is the second such data installment of an all–sky survey of ~ 50 clusters in the redshift range $0.02 \lesssim z \lesssim 0.06$. The data extends the TF study of nearby clusters of Giovanelli *et al.* (1997a,b); they will be used jointly to determine an accurate I band TF template and to establish a cluster inertial reference frame to $z \sim 0.06$.

Subject headings: galaxies: distances and redshifts — cosmology: observations;
distance scale

¹Visiting Astronomer, Kitt Peak National Observatory, National Optical Astronomy Observatories, which are operated by the Association of Universities for Research in Astronomy, Inc., under a cooperative agreement with the National Science Foundation.

²Visiting Astronomer, Cerro Tololo Inter–American Observatory, NOAO.

³Now at European Southern Observatory, Karl Schwarzschild Str. 2, D–85748 Garching b. München, Germany.

1. INTRODUCTION

The accurate measurement of deviations from smooth Hubble flow remains a challenge in observational cosmology. The lack of a proven redshift-independent distance estimator applicable beyond $\sim 100h^{-1}$ Mpc becomes sorely obvious when claims of large amplitude coherent flows on scales larger than this are made (Lauer & Postman 1992:LP; Courteau *et al.* 1993). Recent observational efforts at constructing relations useful for peculiar velocity measurements (e.g. Riess *et al.* 1995 and Giovanelli *et al.* 1996: G96) challenge the LP result, though with insufficient certainty. The Tully–Fisher (TF) sample of G96 peculiar velocities is based on a template defined by 555 galaxies in 24 clusters (Giovanelli *et al.* 1997a,b;G97a,b) that reaches only to $cz \sim 9000$ km s $^{-1}$ and is thus unable to probe the entire peculiar velocity field the LP flow encompasses, whereas the Riess *et al.* sample of supernova type Ia is too sparsely populated to adequately characterize the local bulk flow (Watkins & Feldman 1995). The existing samples of peculiar velocities at relatively large distances ($> 100h^{-1}$) need to be enlarged.

We are expanding upon the data of G97a,b by obtaining TF measurements for an all-sky survey of some 50 clusters in the redshift range $5000 \lesssim cz \lesssim 20,000$ km s $^{-1}$. The benefits of such an enterprise are twofold. First, the combination of our data set with that of G97a,b will yield a highly accurate TF template. The proximity of the extant G97a,b sample allows a wide range of galactic properties to be observed and is thus ideal for determining the slope of the TF relation. On the other hand, the redshifts of our sample of relatively distant clusters are less affected by the vagaries of cosmic peculiar motions, a property useful for accurately extracting the TF magnitude offset. Second, the combined data set will cover a much larger volume than that of G97a,b. Recent work by Scaramella *et al.* (1994), Tini-Brunozzi *et al.* (1995), and Branchini *et al.* (1996) suggests that coherent peculiar motions may persist as far as 18,000 km s $^{-1}$, i.e. the local “convergence depth” may extend to $\sim 180h^{-1}$ Mpc. It thus appears crucial to penetrate the local velocity field as deeply as possible: our sample extends out to and possibly beyond the local convergence depth. This will enable dipole motion measurements over scales large enough to test the LP claim, whose sample has an effective depth of $\sim 100h^{-1}$.

In order to provide public access to the data on the shortest possible time scale, we are presenting results of our survey in installments, as we progress in the data reductions for sizable fractions of the cluster set. Dale *et al.* (1997; hereafter “Paper I”) presented TF measurements for 84 galaxies in the fields of seven Abell clusters. In this paper we present the project’s second data installment: TF measurements for 90 galaxies in the fields of nine Abell clusters, one of which, the field of A2295, contains two separate clusters (see Sec. 3). The following section reviews the imaging and spectroscopic observations for this data

installment. Sec. 3 presents the relevant TF data.

2. OBSERVATIONS

Imaging for this project began in October 1994 and is now complete, whereas spectroscopy measurements began in December 1995 and are still ongoing. In the 50 clusters we have chosen to include in our all-sky survey, we plan to obtain 5 to 15 TF measurements per cluster. Including approximately two dozen 21 cm line widths taken earlier by RG and MH, we have thus far obtained ~ 360 (cluster member) velocity widths in 48 Abell clusters; we expect to measure ~ 100 more velocity widths. Paper III of this series will present the final installment of data for the remaining clusters.

2.1. *I* Band Imaging

All photometric observations were carried out in the *I* band (Kron–Cousins filter, central wavelength of 8075 Å and passband of 1500 Å), matching those in Paper I and G97a,b. The imaging for the clusters in this paper was carried out at the KPNO and CTIO 0.9 m telescopes. Exposures for each frame amounted to 600 seconds, a time sufficient to reliably reach isophotal levels near 24.5 mag arcsec⁻². The clusters A119, A194, A2295, and A2457 were observed at KPNO over the course of several observing runs: October 5–16 1994, September 14–21 1995, September 21–October 1 1995, November 20–26 1995, October 31–November 12 1996, and February 4–19 1997. The clusters A2806, A114, A3193, A3381, and A3744 were observed at CTIO during the runs of February 1–8 1995 and August 28–September 4 1995. We used the same observational methods and technical setups described in Paper I for the KPNO observations; the only significant difference between imaging at KPNO and CTIO for our cluster sample is the higher spatial resolution for the data taken at the CTIO 0.9 m (0.4'' pixel⁻¹ versus 0.68'' pixel⁻¹), and a smaller field of view (14' × 14' versus 23' × 23') for the 2048² CCD. The average seeing FWHM for the images used in this data set was 1.7'' ± 0.2'' at KPNO and 1.4'' ± 0.2'' at CTIO; however, the nights with the best seeing conditions were preferentially devoted to the more distant clusters. The majority of the data presented here were taken in good photometric conditions, for which the photometric zero point calibration could be determined with an accuracy of 0.02 mag or better. In a minority of cases (2%), photometric conditions were of inferior quality. In those cases frames were taken with a substantial sky overlap with images taken in good photometric conditions, so that fluxes of at least 12 field stars could be measured in the overlap region, thus guaranteeing calibration to the ~ 0.03 mag level.

The determination of I band fluxes follows from data reduction methods discussed in Paper I and Haynes *et al.*, in preparation, using both standard and customized IRAF⁴ packages. We will only mention here that the measured fluxes, denoted m_∞ , include extrapolations of the exponential fits to the surface brightness profiles to infinity and are typically accurate to ~ 0.03 mag (uncertainties at least this large are later included after corrections for internal extinction are made; see Paper I for details on flux errors). We apply several corrections to m_∞ , to obtain:

$$m_{\text{cor}} = m_\infty - A_I + k_I - \Delta m_{\text{int}} - \Delta m_T. \quad (1)$$

The first correction, A_I , is for the extinction caused by the Milky Way. We use Burstein and Heiles' (1978) tabulation of galactic extinction values by averaging entries in the *Third Reference Catalogue of Bright Galaxies* (de Vaucouleurs *et al.* 1991) found near the cluster centers. We convert B band results to I band via $A_I = 0.45A_B$; values of A_I for the nine clusters presented here range from 0.00 to 0.17 mag. The internal extinction correction, Δm_{int} , is applied using the procedure outlined in G97a,

$$\Delta m_{\text{int}} = -f(T) \gamma(W_{\text{cor}}) \log(1 - e), \quad (2)$$

where γ ($\lesssim 1.0$) depends on the corrected velocity width W_{cor} (Sec. 2.2) and e is the ellipticity of the spiral disk, corrected for atmospheric seeing effects as described in Sec. 5 of Paper I (the adopted correction Δm_{int} is slightly smaller for early, less dusty galaxies: $f(T)=0.85$ for types T earlier than Sbc; $f(T)=1$ otherwise). We apply a cosmological k-correction: $k_I = (0.5876 - 0.1658T)z$ (Han 1992). Finally, we include a small correction, Δm_T , for the TF dependence on morphological type found in G97b; while the true, unextincted, face-on apparent magnitude of the galaxy is $m_{\text{cor}} + \Delta m_T$, m_{cor} represents the value to be used in TF work with the template TF relation obtained in G97b, characterized for Sbc and Sc galaxies. Thus $\Delta m_T = 0$ for types Sbc and later; the correction is 0.1 mag for Sb types and 0.32 mag for types earlier than Sb.

2.2. Optical Spectroscopy

Rotational velocity widths for this sample of cluster galaxies were extracted from long-slit spectra obtained at the Palomar Observatory 5 m telescope and the CTIO 4 m telescope. The clusters A114, A119, A194, A2295, A3744, and A2457 were observed at Palomar during the runs of October 22–23 1995, December 13–18 1995, July 9–12 1996,

⁴IRAF (Image Reduction and Analysis Facility) is distributed by NOAO.

and September 13–19 1996. The clusters A2806, A3193, and A3381 were observed at CTIO during the nights of April 4–7 1996 and September 30–October 3 1996. We refer the reader to Paper I for details of the spectroscopy performed at Palomar. The observing setup at the CTIO 4 m uses the R–C Spectrograph and the Loral 3k CCD with a 203'' long slit. The combination of the 1200 lines mm^{-1} grating and a 2'' wide slit yields a dispersion of $0.55 \text{ \AA pixel}^{-1}$ and a spectral resolution of 1.7 \AA (equivalent to 75 km s^{-1} at 6800 \AA). Along the cross–dispersion axis, the spatial scale is $0.50'' \text{ pixel}^{-1}$. The wavelength range ($\sim 5640 \text{ \AA}$ to 7320 \AA) is large enough to observe redshifted $\text{H}\alpha$ emission in galaxies with recessional velocities up to $\sim 34,000 \text{ km s}^{-1}$, in our chosen setup.

The adopted observing strategy includes a five minute preliminary integration on each galaxy. This allows a quick estimate of the spectral lines' strength from which we determine the exposure time necessary to adequately sample the outer disk regions. Moreover, performing a five minute test exposure informs us if the galaxy is at the cluster redshift and if the distribution of H II regions is sufficient to provide a useful rotation curve. If the observation is deemed useful, a second integration of usually 15–45 minutes is taken.

We extract optical rotation curves (ORCs) as discussed in Paper I. We use the $\text{H}\alpha$ (6563 \AA) emission line in mapping out the ORC except in 2% of the cases where the emission of the [N II] (6584 \AA) line extends to larger radii than that of the $\text{H}\alpha$ emission. We kinematically center the ORC by assigning the velocity nearest the average of the 10% and 90% velocities to be at radius zero, where an N% velocity is such that N% of the data points in the rotation curve have velocity smaller than it. Besides representing the velocity at the spatial center of the galaxy, we also assume the velocity of the ORC at this radius to be the galaxy's recessional velocity. We define the observed rotational velocity width to be $W_{\text{obs}} \equiv V_{90\%} - V_{10\%}$. In regions where heavy $\text{H}\alpha$ absorption and emission are mixed, usually near the galactic center, we fill in the portions of the rotation curve with data from the [N II] rotation curve, if available. We do this to provide information on the shape of the inner portions of all ORCs and to ensure that our method of computing W_{obs} does not artificially yield slightly large values when data is missing. We apply this [N II] patch to approximately 10% of the $\text{H}\alpha$ ORCs; the notes on individual galaxies in Sec. 3 indicates which ORCs include [N II] patches. In Fig. 1 we display the effect a [N II] patch can have on a ORC using the ORC of galaxy 400641 in Abell 119 as an example. The upper panel gives the $\text{H}\alpha$ ORC without the [N II] patch, the lower panel includes the patch. The effect on the inferred redshift and W_{obs} is small, but the shape of the ORC has changed significantly. This change is in part due to the kinematical recentering of the ORC — the origin of the ORC has also been shifted radially (by $0.94''$). If information on the central portions of an ORC is lacking for all spectral lines available, we consider the peak of the galactic continuum light profile, formed by summing the data along the dispersion direction,

to represent the spatial center of the galaxy (see, for example, the upper panel of Fig. 1).

The method described above on characterizing rotational velocity widths is used since it effectively ignores small-scale velocity irregularities within an ORC that may arise from streaming motions within the galactic disk, the non-uniform distribution of H II regions, or distortions associated with the spiral pattern. Furthermore, we find empirically that provided that the rotation curve extends far enough out into the disk, this method recovers the velocity width at R_{opt} , the distance along the major axis to the isophote containing 83% of the I band flux. This radius is reported by Persic & Salucci (1991 & 1995) to be a useful radius at which to measure the velocity width of ORCs. Thus, extrapolations to the ORC, and hence adjustments to W_{obs} , are made in cases where the ORC’s radial extent falls well short of R_{opt} . The resulting correction which depends on the shape of the rotation curve, Δ_{sh} , rarely exceeds $0.1W_{\text{obs}}$.

To recover the actual velocity widths, two more corrections are necessary. The first is the factor $1/\sin i$ necessary to convert the width observed for a disk inclined to the line of sight at an angle i to what would be observed if the disk were edge-on, and the second is the factor $1/(1+z)$ to correct for the cosmological broadening of W . The corrected optical rotational velocity width is then

$$W_{\text{cor}} = \frac{W_{\text{obs}} + \Delta_{\text{sh}}}{(1+z)\sin i}. \quad (3)$$

A discussion of the errors in the velocity widths can be found in Paper I.

In addition to the 82 ORCs presented here, we also have 21 cm measurements for eight galaxies, all members of Abell 194. Six of the eight H I spectra were taken at the Arecibo Observatory using a spectrometer channel separation of 8 km s^{-1} while the remaining two were obtained at the Greenbank 300’ telescope (Haynes & Giovanelli 1991) at a spectral resolution of 11 km s^{-1} . A typical signal to noise ratio for these observations was 10; errors in the observed velocity widths are of order 15 km s^{-1} . Details on the H I data reduction and the corrections made to the observed velocity widths can be found in G97a. A full discussion of the comparison between H I and optical widths, is given in Giovanelli *et al.* (1997c).

3. DATA

Table 1 lists the main parameters of the clusters. Standard names are listed in column 1. Adopted coordinates of the cluster center are listed in columns 2 and 3, for the epoch 1950; they are obtained from Abell *et al.* (1989), except for the entry A2295b, a system

found to be slightly offset from A2295 in both sky position and redshift. For all the clusters we derived a new systemic velocity, combining the redshift measurements available in the NED⁵ database with our own measurements. These newly determined velocities are listed in columns 4 and 5, in the heliocentric and in the cosmic microwave background (CMB) reference frame (Kogut *et al.* 1993), respectively. We list the number of cluster member redshifts used in determining systemic velocities in column 6. An estimated error for the systemic velocity is parenthesized after the heliocentric figure. Spherical and Cartesian supergalactic coordinates are given in columns 7 and 8, and in columns 9–11, respectively.

Figs. 2–6 show the distribution of the galaxies in each cluster. The top panel in each of these figures displays the spatial location of: the outline of the fields imaged (large squares), cluster members (circles — those with poor/unusable velocity widths are left unfilled), background or foreground objects (asterisks), and galaxies with known redshift but without reliable widths (dots). Circles of 1 and 2 Abell radii, R_A , are drawn as dashed lines, if the area displayed is large enough. If no dashed circle is drawn, R_A is larger than the figure limits. We also plot radial (CMB) velocity as a function of angular distance from the cluster center in the lower panel of each figure. A dashed vertical line is drawn at 1 R_A . The combination of the sky and velocity plots is used to gauge cluster membership for each galaxy.

We separate photometric data and spectroscopic data in two tables. Table 2 lists the spectroscopic properties and Table 3 gives the pertinent photometric results.

Entries in the tables are sorted first by the Right Ascension of each cluster, and within each cluster sample by increasing galaxy Right Ascension. The listed parameters for Table 2 are:

Col 1: identification names corresponding to a coding number in our private database, referred to as the Arecibo General Catalog, which we maintain for easy reference in case readers may request additional information on the object.

Cols. 2 and 3: Right Ascension and Declination in the 1950.0 epoch. Coordinates have been obtained from the Digitized Sky Survey catalog and are accurate to $< 2''$.

Cols. 4 and 5: the galaxy radial velocity as measured in the heliocentric and CMB reference frame (Kogut *et al.* 1993). Errors are parenthesized: e.g. 13241(08) implies 13241 ± 08 .

Col. 6: the raw velocity width in km s^{-1} . Measurement of optical widths are described in

⁵The NASA/IPAC Extragalactic Database is operated by the Jet Propulsion Laboratory, California Institute of Technology, under contract with the National Aeronautics and Space Administration.

Sec. 2.2; 21 cm line widths are denoted with a dagger and refer to values measured at a level of 50% of the profile horns.

Col. 7: the velocity width in km s^{-1} after correcting for ORC shape, the cosmological stretch of the data and, for 21 cm data, signal to noise effects, interstellar medium turbulence, and instrumental and data processing broadening; details on the adopted corrections for optical and 21 cm data are given in Sec. 2.2 and G97a, respectively.

Col. 8: the corrected velocity width in km s^{-1} converted to an edge-on perspective.

Col. 9: the adopted inclination i of the plane of the disk to the line of sight, in degrees, (90° corresponding to edge-on perspective); the derivation of i and its associated uncertainty are discussed in Sec. 4 of Paper I.

Col. 10: the logarithm in base 10 of the corrected velocity width (value in column 7), together with its estimated uncertainty between brackets. The uncertainty takes into account both measurement errors and uncertainties arising from the corrections. The format 2.576(22), for example, is equivalent to 2.576 ± 0.022 .

The position angle adopted for the slit of each spectroscopic observation is that given in column 4 of Table 3. The first column in Table 3 matches that of Table 2. The remaining listed parameters for Table 3 are:

Col. 2: morphological type code in the RC3 scheme, where code 1 corresponds to Sa's, code 3 to Sb's, code 5 to Sc's and so on. When the type code is followed by a "B", the galaxy disk has an identifiable bar. We assign these codes after visually inspecting the CCD I band images and after noting the value of R_{75}/R_{25} , where R_X is the radius containing X% of the I band flux. This ratio is a measure of the central concentration of the flux which was computed for a variety of bulge-to-disk ratios. Given the limited resolution of the images, some of the inferred types are rather uncertain; uncertain types are followed by a colon.

Col. 3: the angular distance θ in arcminutes from the center of each cluster.

Col. 4: position angle of the major axis of the image, also used for spectrograph slit positioning (North: 0° , East: 90°).

Col. 5: observed ellipticity of the disk.

Col. 6: ellipticity corrected for seeing effects as described in Sec. 5 of Paper I, along with its corresponding uncertainty. The format 0.780(16), for example, is equivalent to 0.780 ± 0.016 .

Col. 7: surface brightness of the disk at zero radius, as extrapolated from the fit to the disk surface brightness profile.

Col. 8: the (exponential) disk scale length.

Col. 9: the distance along the major axis to the isophote containing 83% of the I band flux.

Col. 10: isophotal radius along the major axis where the surface brightness equals $23.5 \text{ mag sec}^{-2}$.

Col. 11: apparent magnitude within the $23.5 \text{ mag sec}^{-2}$ isophote.

Col. 12: the measured I band magnitude, extrapolated to infinity assuming that the surface brightness profile of the disk is well described by an exponential function.

Col. 13: the apparent magnitude, to which k -term, galactic and internal extinction corrections were applied; details on the adopted corrections are given in Sec. 2.1.

Col. 14: the absolute magnitude, computed assuming that the galaxy is at the distance indicated either by the cluster redshift, if the galaxy is a cluster member within $1 R_A$ of the cluster center, or by the galaxy redshift if not. The calculation assumes $H_o = 100h \text{ km s}^{-1} \text{ Mpc}^{-1}$, so the value listed is strictly $M_{\text{cor}} - 5 \log h$. In calculating this parameter, radial velocities are expressed in the CMB frame and uncorrected for any cluster peculiar motion. The uncertainty on the magnitude, indicated between brackets in hundredths of a mag, is the sum in quadrature of the measurement errors and the estimate of the uncertainty in the corrections applied to the measured parameter.

When an asterisk appears at the end of the record, a detailed comment is given for that particular object. Because of the length and number of these comments, they are not appended to the table but included in the text as follows. Note that a record is flagged in both tables 2 and 3, independently on whether the comments refer only to the photometry, only to the spectroscopy, or both.

A2806:

20391: possible disk warp; [N II] patch for radii $< 8''$

400698: mostly bulge ORC; uncert. extrap.

400703: mostly bulge ORC; uncert. extrap.; unfit for TF use.

400713: mostly bulge ORC; large extrap.; exp. disk over narrow range of radii.

A114:

400672: exp. disk over narrow range of radii.

400443: uncert. ellipticity; $H\alpha$ absorption in bulge – [N II] patch for radii $< 3''$; two nuclei?

400453: uncert. PA.

A119:

400619: exp. disk over narrow range of radii; $H\alpha$ absorption in bulge – [N II] patch for radii $< 2.5''$.

400600: uncert. ORC extrap.; [N II] line used.
400641: uncert. ellipticity; [N II] patch for radii $\lesssim 2''$.
400658: background gal.

A194:

784: only 21 cm width available.
830: only 21 cm width available; note low i ; unfit for TF use.
894: foreground gal.; only 21 cm width available.
915: background gal.; only 21 cm width available.
931: foreground gal.; only 21 cm width available.
410584: asymm. nucleus.
1116: only 21 cm width available.
1120: only 21 cm width available.
1123: only 21 cm width available.

A3193:

23113: note low i .
23130: extremely low surf. brightness at radii $\gtrsim 20''$; heavy H α absorption throughout disk; unfit for TF use.
23136: note low i ; [N II] patch for radii $\lesssim 0.5''$.

A3381:

460069: rising ORC; uncert. extrap.
460071: H α absorption in bulge.
24895: companion galaxy $35''$ to SE.

A2295b:

270370: rising ORC; uncert. extrap.; uncertain PA.
280128: mostly bulgy ORC.
280130: star $40''$ to WNW.
280134: foreground gal.

A2295:

270375: rising ORC; note low i ; small companion gal $10''$ to E.; unfit for TF use; 5 min. integ.
280131: background gal.
280136: background gal.

A3744:

610196: rising ORC; large extrap.
610198: rising ORC.
34131: faint disk; large extrapolation made to ORC.
610220: heavy H α absorption in one half of disk.
610222: slightly rising ORC.

34189: foreground gal.; patchy H II distribution.

610251: foreground gal.

A2457:

320572: mostly bulge ORC; large correction applied to W_{ORC} ; [N II] line used.

320573: outer isophotes differ in ell., PA w.r.t. inner isophotes.

320574: background gal.

320576: star 55" to NE; uncert. ellipticity; [N II] patch for radii $\lesssim 1.5''$.

320579: slightly rising ORC; uncert. ellipticity; [N II] patch for $2'' \lesssim$ radii $\lesssim 4''$.

320581: [N II] patch for radii $\lesssim 2''$.

320583: asymm; merger?

320591: foreground gal.; 5 min. integ.

In Fig. 7, we plot the ORCs folded about a kinematic center as described in Sec. 2.2. The horizontal dashed line in each panel indicates the adopted (and uncorrected for inclination) half velocity width, $W/2$, for each galaxy and the vertical dashed line is drawn at R_{opt} . We have overlaid fits to the ORCs for the cases in which shape corrections to the velocity widths are necessary. Finally, in Fig. 8 we give, as an example, the surface brightness profiles for the first 16 galaxies in Fig. 7. Again the vertical dashed line refers to R_{opt} . The solid line drawn along the disk is the fit to the disk over the range of radii assumed to cover the exponential portion of the disk. The remainder of the plots of surface brightness profiles for the complete sample can be obtained by contacting the first author.

Fig. 9 gives the “raw” TF plots of each cluster uncorrected for any cluster incompleteness bias. A computation of such bias will be presented in future work when data from all clusters is in hand. Furthermore, the cluster systemic redshifts used in obtaining these plots are preliminary. Included in the TF plots is the template relation obtained from nearby clusters in G97b:

$$y = -7.68x - 21.01 \tag{4}$$

where y is $M_{\text{cor}} - 5\log h$ and x is $\log W_{\text{cor}} - 2.5$.

We thank Katie Jore for the use of her ORC fitting programs. The results presented here are based on observations carried out at the Palomar Observatory (PO), at the Kitt Peak National Observatory (KPNO), at the Cerro Tololo Inter-American Observatory (CTIO), the (late) 300' telescope of the National Radio Astronomy Observatory (NRAO), and the Arecibo Observatory, which is part of the National Astronomy and Ionosphere Center (NAIC). KPNO AND CTIO are operated by Associated Universities for Research in Astronomy and NAIC is operated by Cornell University, all under cooperative agreements with the National Science Foundation. The Hale telescope at the PO is operated by the

California Institute of Technology under a cooperative agreement with Cornell University and the Jet Propulsion Laboratory. The National Radio Astronomy Observatory (NRAO) is operated by Associated Universities, Inc. under a management agreement with NSF. This research was supported by NSF grants AST94-20505 to RG and AST95-28960 to MH. LEC was partially supported by FONDECYT grant #1970735.

REFERENCES

- Abell, G., Corwin, H.G. & Olowin, R.P. 1989, ApJS, 70, 1
- Branchini, E., Plionis, M. & Sciama, D.W. 1996, ApJ, 461, L17
- Courteau, S., Faber, S., Dressler, A. & Willick, J. 1993, ApJ, 412, L51
- Dale, D., Giovanelli, R., Haynes, M., Scodreggio, M., Hardy, E. & Campusano, L. 1997, AJ, 114, 455 [Paper I]
- de Vaucouleurs, G., de Vaucouleurs, A., Corwin, H. G., Buta, R. J., Paturel, G. & Fouque, P. 1991, *Third Reference Catalogue of Bright Galaxies*, (New York: Springer)
- Giovanelli, R., Haynes, M.P., Wegner, G., da Costa, L.N., Freudling, W. and Salzer, J.J. 1996, ApJ 464, L99 [G96]
- Giovanelli, R., Haynes, M.P., Herter, T., Vogt, N.P., Wegner, G., Salzer, J.J., da Costa, L.N. & Freudling, W. 1997, AJ, 113, 22 [G97a]
- Giovanelli, R., Haynes, M.P., Herter, T., Vogt, N.P., da Costa, L.N., Freudling, W., Salzer, J.J. & Wegner, G. 1997, AJ, 113, 53 [G97b]
- Giovanelli, R., Haynes, M.P., Dale, D.A., & Hardy, E. 1997c, in preparation
- Han, M. 1992, ApJS, 81, 35
- Haynes, M.P. and Giovanelli, R. 1991, ApJS, 77, 331
- Kogut, A. *et al.* 1993, ApJ, 419, 1
- Lauer, T. & Postman, M. 1994, ApJ, 425, 418
- Persic, M. & Salucci, M. 1991, ApJ, 368, 60
- Persic, M. & Salucci, M. 1995, ApJS, 99, 501

Riess, A., Press, W. & Kirshner, R. 1995, ApJ, 445, L91

Scaramella, R., Vettolani, G. & Zamorani, G. 1994, ApJ, 422, 1

Tini–Brunozzi, P., Borgani, S., Plionis, M., Moscardini, L. & Coles, P. 1995, MNRAS, 277, 1210

Tully, R.B. & Fisher, J.R. 1977, A&A, 54, 661

Watkins, R. & Feldman, H. 1995, ApJ, 453, L73

Fig. 1.— The effect of a [N II] data patch on a kinematically folded H α rotation curve lacking data in the central regions due to absorption. The upper panel displays the H α rotation curve for galaxy 400641 in Abell 119 without the patch, the lower panel includes the [N II] data patch. Notice the kinematical recentering changes the definition of the ORC origin in the spatial direction as well as in the velocity direction.

Fig. 2.— Sky and velocity distribution of galaxies in the clusters Abell 2806 and Abell 114. Circles represent cluster members with measured photometry and widths; if unfilled, widths are poorly determined. Asterisks identify foreground and background galaxies and dots give the location of galaxies with known redshift, but lacking accurate width and/or photometry. Large square boxes indicate outlines of imaged fields with the 0.9 m telescope. Vertical dashed lines in the lower panels indicate $1 R_A$ (and $2 R_A$ for A114). The upper panels contain circles of radius $1 R_A$ (and $2 R_A$ for A114).

Fig. 3.— Sky and velocity distribution of galaxies in the clusters Abell 119 and Abell 194. Filled circles, unfilled circles, asterisks, dots, large squares and dashed lines and circles follow the same convention as in Fig. 2.

Fig. 4.— Sky and velocity distribution of galaxies in the clusters Abell 3193 and Abell 3381. Filled circles, unfilled circles, asterisks, dots, large squares and dashed lines and circles follow the same convention as in Fig. 2.

Fig. 5.— Sky and velocity distribution of galaxies in the clusters Abell 2295, Abell 2295b, and Abell 3744. For A2295 and A3744, filled circles, unfilled circles, asterisks, dots, large squares and dashed lines and circles follow the same convention as in Fig. 2. For A2295b, filled triangles identify cluster members and $1 R_A$ is indicated by the dotted line in the lower panel and by the dotted circle of radius $1 R_A$ in the upper panel.

Fig. 6.— Sky and velocity distribution of galaxies in the cluster Abell 2457. Filled circles, unfilled circles, asterisks, dots, large squares and dashed lines and circles follow the same convention as in Fig. 2.

Fig. 7.— H α rotation curves for 82 galaxies (except for galaxies 400600 and 320572, for which the ORCs are obtained from a [N II] emission line), folded about the kinematic centers. The error bars include both the uncertainty in the wavelength calibration and the ORC fitting routine used. Names of the galaxy and the corresponding parent cluster are given along with the CMB radial velocity. Two dashed lines are drawn: the horizontal line indicates the adopted half velocity width, $W/2$, which in some cases arises from an extrapolation to the ORC or from a 21 cm width (see Table 2); the vertical line is at R_{opt} , the radius containing 83% of the I band flux. For those cases where a shape correction to the velocity width is

used, a fit to the ORC is indicated by a solid line. Note that the rotation curves are *not* deprojected to an edge-on orientation.

Fig. 8.— A sampling of surface brightness profiles. Names of the galaxy and the corresponding parent cluster are given in each panel. Two lines are drawn: the vertical dashed line is drawn at R_{opt} and the solid line is an exponential fit to the disk, over the range of radii over which the disk is assumed to behave exponentially.

Fig. 9.— “Raw” TF plots for the 10 clusters are given. We emphasize that the data have *not* been corrected for incompleteness bias. In the A2295 panel, the error bars containing filled circles represent members of “A2295b,” a cluster at a lower redshift than A2295. The dashed line is the template relation valid for low z clusters, Eqn. (4).

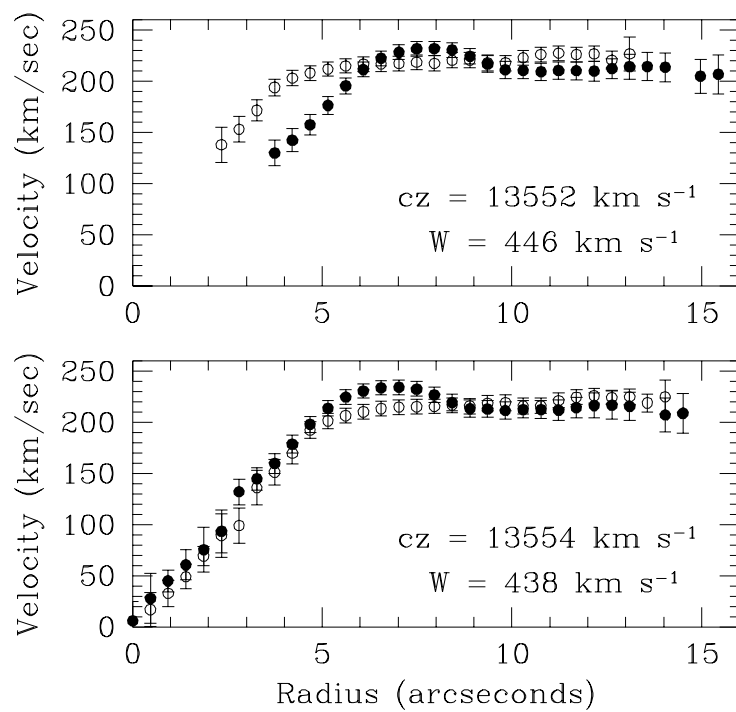


fig. 1

TABLE 1. Cluster Coordinates

Cluster	R.A.	Decl.	V_{\odot}	V_{cmb}	N_z	SGL	SGB	X	Y	Z
	<i>h m s</i>	<i>d m s</i>	<i>km s⁻¹</i>	<i>km s⁻¹</i>		$^{\circ}$	$^{\circ}$	<i>km s⁻¹</i>	<i>km s⁻¹</i>	<i>km s⁻¹</i>
(1)	(2)	(3)	(4)	(5)	(6)	(7)	(8)	(9)	(10)	(11)
A2806	003754	-562600	8062(92)	7910	23	240.9	-11.0	-3774	-6787	-1505
A 114	005112	-215700	17436(143)	17144	41	275.4	-5.4	1615	-16990	-1624
A 119	005348	-013200	13377(153)	13048	37	295.3	-0.7	5581	-11793	-151
A 194	012300	-014600	5300(43)	4995	100	-62.9	-7.8	2252	-4407	-674
A3193	035654	-522900	10390(102)	10354	25	239.9	-39.5	-4001	-6916	-6585
A3381	060806	-333500	11451(49)	11551	37	234.0	-69.4	-2383	-3287	-10814
A2295b	175900	+691600	18701(82)	18633	6	32.5	35.7	12753	8139	10877
A2295	180018	+691300	24623(199)	24555	9	32.4	35.8	16858	10710	14402
A3744	210418	-254100	11692(61)	11429	57	244.9	37.7	-3828	-8189	6993
A2457	223312	+011300	17712(119)	17349	14	287.5	33.8	4327	-13751	9653

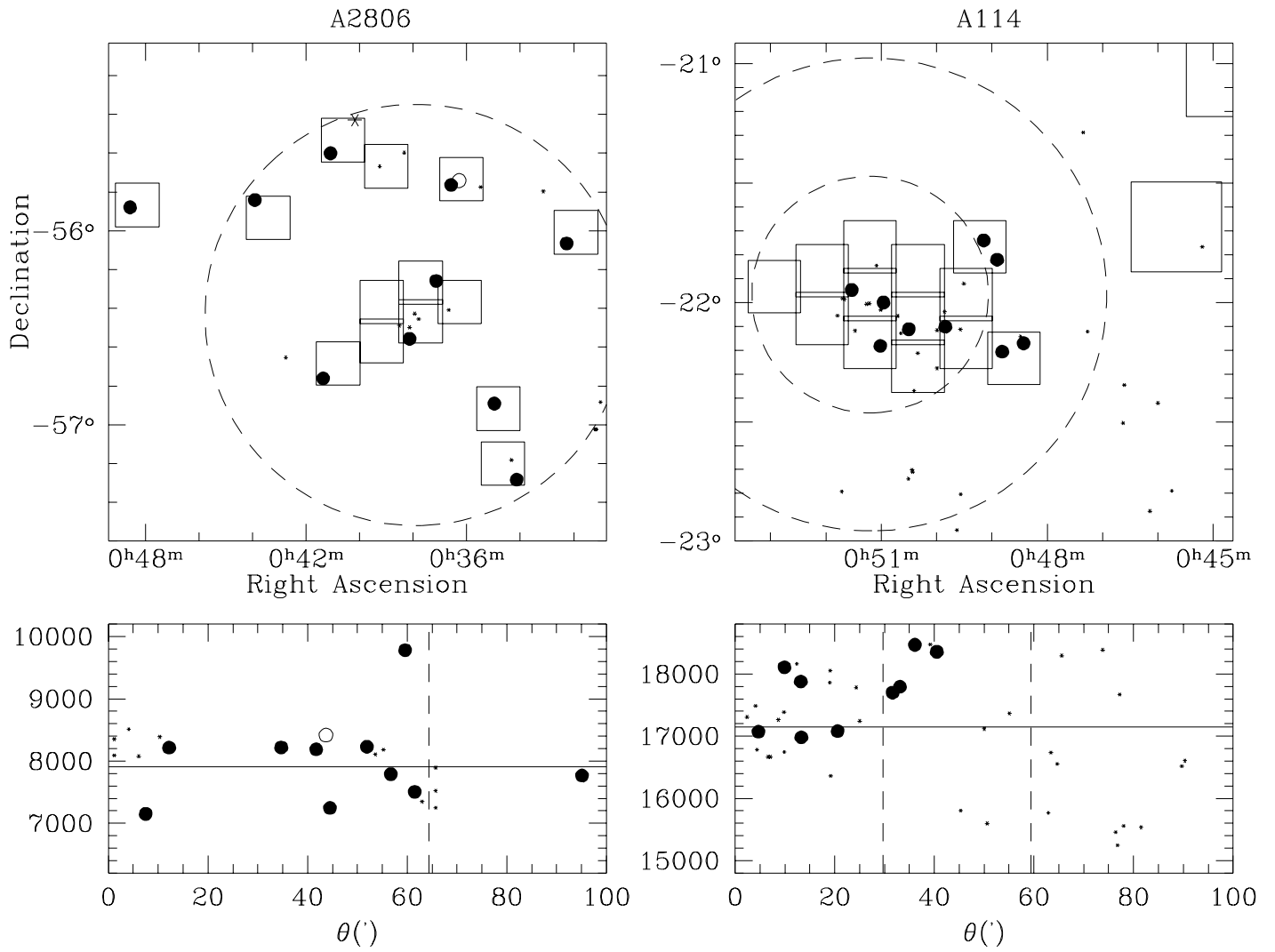


fig. 2

TABLE 2. (continued)

Names	R.A. <i>h m s</i>	Dec. <i>d m s</i>	V_{\odot} <i>km s⁻¹</i>	V_{cmb} <i>km s⁻¹</i>	W_{obs} —	W <i>km s⁻¹</i>	W_{cor} —	i °	$\log W_{\text{cor}}$
(1)	(2)	(3)	(4)	(5)	(6)	(7)	(8)	(9)	(10)
320591	223417.2	+012219	11300(08)	10937	380	367	367	86	2.565(18) *

†21cm data

TABLE 2. (continued)

Names	R.A.	Dec.	V_{\odot}	V_{cmb}	W_{obs}	W	W_{cor}	i	$\log W_{\text{cor}}$
(1)	$h m s$	$d m s$	$km s^{-1}$	$km s^{-1}$	-	$km s^{-1}$	-	$^{\circ}$	(10)
270378	175910.3	+690545	24513(07)	24445	353	350	351	84	2.546(24)
270379	175920.9	+690146	24410(07)	24342	328	303	326	69	2.513(15)
280122	180006.7	+691127	23744(10)	23676	456	423	436	76	2.640(16)
280126	180108.3	+691926	25236(07)	25167	476	439	485	65	2.686(13)
280131	180210.3	+684236	27425(07)	27355	560	513	518	83	2.714(11) *
280132	180211.5	+691430	25391(07)	25322	335	309	329	70	2.517(16)
280133	180335.0	+691651	24728(07)	24658	434	404	432	69	2.636(23)
280136	180446.6	+691521	27367(07)	27296	370	339	362	70	2.558(16) *
A3744									
610196	210224.6	-254603	11234(07)	10972	171	230	232	82	2.365(65) *
610198	210243.2	-254505	12171(07)	11909	128	144	146	82	2.163(41) *
34131	210328.5	-243358	11077(07)	10811	186	186	206	65	2.314(69) *
34135	210331.0	-243649	11160(09)	10894	365	382	414	68	2.617(28)
610212	210336.2	-244122	10394(07)	10128	194	201	202	87	2.304(34)
610214	210344.2	-254001	11298(07)	11035	295	285	285	88	2.454(25)
610217	210405.5	-244917	11312(07)	11046	234	226	232	76	2.366(28)
610220	210415.7	-252716	11602(10)	11338	307	296	329	64	2.517(29) *
610222	210425.0	-254955	12204(07)	11941	383	381	384	83	2.584(24) *
610224	210427.7	-254623	12740(07)	12477	201	206	214	75	2.331(30)
610231	210444.0	-245130	11145(08)	10879	378	365	415	61	2.619(22)
34189	210611.4	-254532	8793(09)	8529	224	218	221	80	2.345(45) *
610251	210620.6	-254550	8876(07)	8611	153	153	153	85	2.185(42) *
A2457									
320569	223129.7	+013929	18084(07)	17721	551	520	535	77	2.728(12)
320572	223157.3	+011808	18281(08)	17918	433	452	454	85	2.657(33) *
320573	223159.2	+010926	17815(07)	17452	343	329	357	67	2.552(25) *
320574	223203.8	+014007	20992(08)	20629	399	373	377	82	2.577(16) *
320575	223210.5	+010602	17779(07)	17416	500	473	475	84	2.677(17)
320576	223236.9	+010514	18254(07)	17891	417	394	495	53	2.695(53) *
320578	223237.2	+003515	17786(08)	17424	398	376	377	87	2.576(16)
320579	223301.0	+013603	16777(07)	16414	281	276	310	63	2.492(32) *
320581	223308.8	+012401	16933(07)	16570	531	503	560	64	2.748(15) *
320583	223333.7	+011759	16023(07)	15660	358	340	351	76	2.545(22) *

TABLE 2. (continued)

Names	R.A. <i>h m s</i>	Dec. <i>d m s</i>	V_{\odot} <i>km s⁻¹</i>	V_{cmb} <i>km s⁻¹</i>	W_{obs} –	W <i>km s⁻¹</i>	W_{cor} –	i °	$\log W_{\text{cor}}$
(1)	(2)	(3)	(4)	(5)	(6)	(7)	(8)	(9)	(10)
894	011847.4	-001015	3790(07)	3479	192 [†]	166	178	69	2.250(35) *
915	011950.5	-010808	8145(04)	7836	561 [†]	516	560	67	2.748(15) *
931	012041.2	-005741	2001(04)	1692	121 [†]	103	105	78	2.023(56) *
410188	012300.2	-020418	6416(07)	6111	155	160	181	62	2.259(34)
410583	012601.2	-020905	4978(07)	4675	184	181	189	74	2.276(38)
1060	012622.8	-020439	4787(07)	4484	233	230	240	73	2.380(22)
410584	012653.3	-012728	4909(07)	4606	248	244	249	79	2.397(23) *
1116	013101.5	-012047	4720(25)	4421	284 [†]	259	263	80	2.420(75) *
1120	013129.3	-011953	4664(08)	4365	371 [†]	340	346	79	2.539(20) *
1123	013134.8	-011715	4916(20)	4618	448 [†]	430	432	84	2.636(40) *
A3193									
430691	035536.4	-523241	10148(07)	10111	264	255	282	65	2.450(31)
430695	035638.0	-522350	9720(10)	9683	216	213	251	58	2.399(35)
430697	035704.9	-521655	10299(07)	10262	394	381	393	76	2.594(21)
430698	035737.0	-524145	10458(07)	10423	177	181	187	76	2.271(29)
23113	035822.6	-524916	9796(07)	9762	212	205	327	39	2.515(78)
23130	035923.4	-525222	10569(07)	10536	255	257	308	56	2.489(42) *
23136	040000.5	-525044	9965(07)	9932	391	378	519	47	2.715(27) *
A3381									
460069	060740.0	-333701	11199(07)	11298	378	389	404	75	2.606(35) *
460070	060740.7	-333230	10309(08)	10408	307	297	308	75	2.488(26)
460071	060749.2	-333435	11149(07)	11249	285	285	315	65	2.498(36) *
460077	060832.3	-334045	9004(07)	9105	287	279	334	57	2.523(25)
24895	060915.8	-331718	11517(07)	11619	342	330	347	72	2.540(33) *
A2295b									
270368	175613.4	+690321	18844(07)	18778	274	258	289	63	2.461(31)
270370	175636.9	+690315	18835(10)	18769	277	297	298	88	2.474(39) *
280128	180121.3	+692935	18535(07)	18466	385	367	378	76	2.578(23) *
280130	180209.7	+693046	18482(07)	18413	474	447	537	56	2.730(28) *
280134	180410.5	+692240	15740(07)	15670	433	411	418	80	2.621(15) *
A2295									
270373	175823.3	+690435	25332(07)	25265	322	297	340	61	2.532(20)
270375	175826.1	+691738	24430(07)	24363	270	277	473	36	2.675(58) *

TABLE 2. Galaxy Spectroscopic Parameters, by Cluster

Names	R.A.	Dec.	V_{\odot}	V_{cmb}	W_{obs}	W	W_{cor}	i	$\log W_{\text{cor}}$
(1)	$h\ m\ s$	$d\ m\ s$	$km\ s^{-1}$	$km\ s^{-1}$	–	$km\ s^{-1}$	–	$^{\circ}$	(10)
A2806									
20391	003216.2	-560354	8387(13)	8231	494	502	516	77	2.713(18) *
400697	003407.7	-571700	9928(10)	9779	293	284	286	83	2.456(28)
400698	003458.0	-565327	7400(08)	7249	242	265	278	72	2.444(35) *
400703	003616.6	-554427	8574(12)	8417	208	218	279	51	2.446(63) *
400704	003635.1	-554548	8344(08)	8188	172	167	200	57	2.301(32)
400706	003708.4	-561531	8370(07)	8216	229	223	227	79	2.356(23)
400713	003808.0	-563316	7304(07)	7152	196	221	241	66	2.382(44) *
20487	004105.0	-553601	7948(07)	7792	406	396	414	73	2.617(16)
400727	004121.6	-564538	8369(07)	8219	248	241	248	77	2.394(26)
20512	004354.4	-555028	7660(07)	7506	414	404	413	78	2.616(17)
20587	004834.3	-555244	7919(07)	7767	425	414	421	80	2.624(17)
A114									
400421	004825.6	-221015	18649(07)	18356	546	514	527	78	2.722(11)
400672	004848.8	-221222	18760(07)	18467	289	272	284	74	2.453(15) *
400673	004854.3	-214915	18092(07)	17798	272	270	287	70	2.458(25)
400674	004908.9	-214423	17989(08)	17695	196	195	196	84	2.291(32)
400443	004950.5	-220606	17373(07)	17081	356	337	427	52	2.630(54) *
400453	005028.2	-220644	17274(07)	16982	377	357	387	67	2.588(14) *
400686	005057.6	-220716	18401(07)	18109	409	386	400	75	2.602(14)
400466	005100.9	-221055	18169(07)	17878	448	423	453	69	2.656(13)
400688	005132.0	-215652	17364(07)	17072	344	325	347	70	2.540(19)
A119									
400611	005208.8	-014537	11860(08)	11530	508	489	507	75	2.705(16)
400619	005240.2	-012048	14306(07)	13976	391	374	382	78	2.582(17) *
400600	005405.6	-013355	15036(10)	14707	367	363	377	75	2.576(22) *
400641	005413.3	-015201	13554(08)	13226	438	419	462	65	2.665(21) *
400653	005526.5	-014121	13073(07)	12745	286	274	278	81	2.444(17)
400658	005623.9	-005531	22779(07)	22451	414	385	416	68	2.619(14) *
A194									
784	011131.1	-020022	4901(05)	4586	299 [†]	268	299	64	2.476(22) *
830	011518.4	-021312	5954(06)	5642	109 [†]	90	154	36	2.188(67) *
847	011630.8	-002405	5218(08)	4905	249	254	254	90	2.405(29)

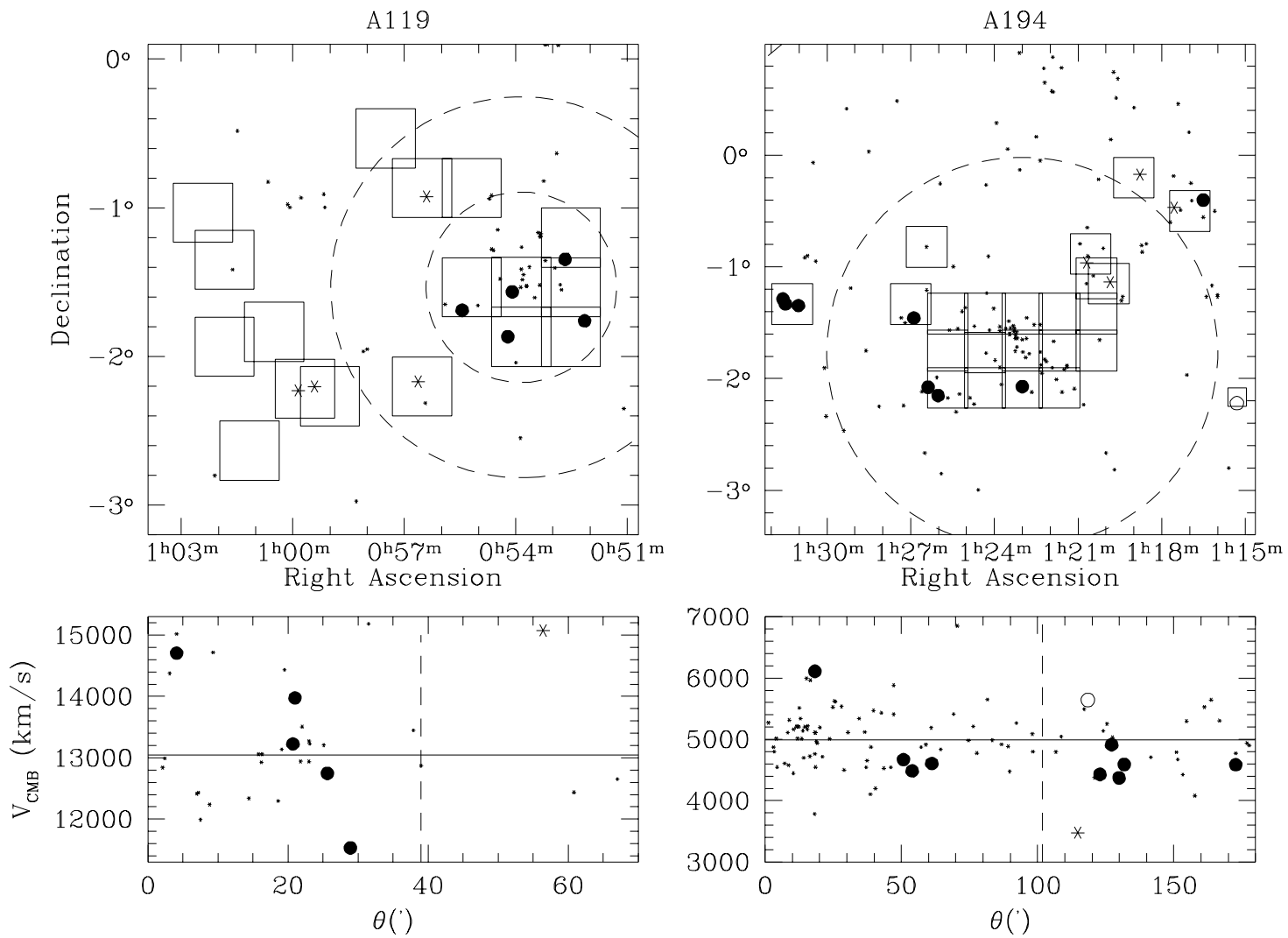


fig. 3

TABLE 3. (continued)

Names	T	θ '	PA °	ϵ	ϵ_{cor}	$\mu(0)$	R_d "	R_{opt} "	$R_{23.5}$ "	$m_{23.5}$	m_∞	m_{cor}	M_{cor}
(1)	(2)	(3)	(4)	(5)	(6)	(7)	(8)	(9)	(10)	(11)	(12)	(13)	(14)
320591	5	19	92	0.819	0.856(08)	18.6	5.8	19.6	25.8	14.96	14.90	14.04	-21.16(14) *

TABLE 3. (continued)

Names	T	θ '	PA °	ϵ	ϵ_{cor}	$\mu(0)$	R_d "	R_{opt} "	$R_{23.5}$ "	$m_{23.5}$	m_∞	m_{cor}	M_{cor}
(1)	(2)	(3)	(4)	(5)	(6)	(7)	(8)	(9)	(10)	(11)	(12)	(13)	(14)
270378	5	9	40	0.765	0.836(11)	19.1	2.7	9.5	12.2	16.54	16.48	15.71	-21.24(13)
270379	5	12	45	0.568	0.616(23)	20.2	2.7	7.4	8.3	16.88	16.75	16.42	-20.53(06)
280122	4:	2	93	0.664	0.722(15)	18.8	2.8	9.3	12.3	15.90	15.83	15.40	-21.55(11)
280126	3	8	59	0.511	0.538(13)	19.4	4.3	13.0	16.0	15.00	14.91	14.56	-22.39(06)
280131	1	32	151	0.718	0.763(10)	18.5	3.8	12.3	17.2	15.24	15.19	14.35	-22.84(12) *
280132	5	10	100	0.570	0.635(13)	18.9	2.0	6.8	8.6	16.66	16.58	16.24	-20.71(06)
280133	4:	18	66	0.584	0.623(18)	20.8	4.0	8.4	10.0	16.26	16.11	15.80	-21.15(05)
280136	4	24	17	0.568	0.631(15)	18.4	2.4	9.0	11.1	15.99	15.90	15.55	-21.63(06) *
A3744													
610196	5	26	70	0.791	0.816(15)	20.4	7.9	24.9	25.1	15.59	15.45	14.74	-20.55(13) *
610198	6	22	26	0.770	0.816(14)	20.4	4.2	12.1	12.1	17.20	17.00	16.47	-18.82(12) *
34131	4:	68	20	0.547	0.557(21)	21.0	8.5	33.3	18.4	15.80	15.36	14.96	-20.21(15) *
34135	4	65	120	0.569	0.599(24)	15.4	3.2	18.8	23.9	13.48	13.44	13.11	-22.07(07)
610212	5	60	102	0.816	0.857(14)	18.9	3.7	13.2	15.5	16.47	16.38	15.57	-19.46(13)
610214	5	8	30	0.826	0.864(08)	19.7	6.7	18.3	23.3	15.42	15.34	14.45	-20.84(14)
610217	4	52	98	0.696	0.731(12)	20.6	5.5	14.1	14.8	16.19	16.01	15.43	-19.79(11)
610220	1	14	80	0.496	0.528(19)	18.5	3.2	10.2	15.1	14.65	14.60	13.98	-21.31(08) *
610222	5	9	73	0.745	0.817(30)	14.3	2.3	15.2	19.4	14.31	14.28	13.55	-21.74(15) *
610224	5	6	45	0.672	0.706(15)	19.7	4.2	11.8	14.6	15.90	15.80	15.26	-20.03(10)
610231	3	50	27	0.470	0.490(11)	19.5	4.9	14.6	18.1	14.72	14.61	14.26	-20.92(07)
34189	5	26	165	0.766	0.781(16)	20.6	11.3	25.5	29.9	14.63	14.49	13.84	-20.81(11) *
610251	6	28	10	0.807	0.848(10)	19.7	4.3	11.9	14.5	16.72	16.63	16.04	-18.63(11) *
A2457													
320569	1	37	26	0.679	0.697(18)	20.8	9.5	21.1	25.0	14.48	14.34	13.65	-22.59(08)
320572	5	19	79	0.810	0.846(11)	18.5	5.7	18.0	26.2	14.63	14.58	13.71	-22.48(15) *
320573	4	19	14	0.544	0.595(55)	18.4	2.3	7.9	10.2	15.19	15.15	14.81	-21.38(06) *
320574	5	32	161	0.753	0.807(11)	19.5	3.6	10.6	14.4	15.93	15.84	15.16	-21.41(12) *
320575	4:	17	6	0.791	0.832(07)	18.9	4.7	12.2	20.0	15.25	15.23	14.42	-21.78(14)
320576	4:	12	93	0.375	0.384(92)	20.0	8.9	25.0	25.6	13.94	13.81	13.61	-22.59(06) *
320578	5	39	116	0.809	0.857(09)	18.9	4.4	14.2	19.1	15.61	15.55	14.69	-21.52(14)
320579	4B	23	72	0.490	0.529(54)	18.4	2.7	11.2	12.6	15.32	15.23	14.84	-21.35(07) *
320581	1	11	6	0.496	0.527(10)	18.6	3.5	10.2	16.0	14.41	14.36	13.77	-22.43(07) *
320583	4:	7	10	0.682	0.728(10)	18.8	3.4	10.4	14.9	15.36	15.31	14.83	-21.37(09) *

TABLE 3. (continued)

Names	T	θ '	PA °	ϵ	ϵ_{cor}	$\mu(0)$	R_d "	R_{opt} "	$R_{23.5}$ "	m _{23.5}	m _∞	m _{cor}	M _{cor}
(1)	(2)	(3)	(4)	(5)	(6)	(7)	(8)	(9)	(10)	(11)	(12)	(13)	(14)
894	5:	115	105	0.598	0.619(13)	18.0	5.6	22.5	28.2	13.93	13.87	13.52	-19.19(05) *
915	4	61	132	0.584	0.592(12)	18.5	14.3	48.5	66.6	11.86	11.80	11.51	-22.96(04) *
931	5	59	7	0.736	0.753(09)	20.3	9.8	28.5	28.6	14.99	14.78	14.37	-16.77(07) *
410188	5	18	4	0.479	0.512(27)	18.8	3.8	14.7	18.1	14.78	14.70	14.43	-19.07(05)
410583	5	51	22	0.632	0.692(14)	18.8	3.0	9.5	13.1	15.71	15.65	15.23	-18.26(06)
1060	5	54	82	0.656	0.682(13)	19.6	7.1	21.1	25.2	14.69	14.58	14.10	-19.39(07)
410584	4	61	74	0.737	0.764(13)	19.1	6.0	17.3	24.4	14.53	14.45	13.86	-19.64(09) *
1116	5	123	115	0.761	0.786(31)	18.3	7.2	25.4	34.3	13.77	13.73	13.05	-20.18(11) *
1120	2	130	138	0.712	0.730(10)	18.6	8.9	27.1	40.1	12.96	12.91	12.17	-21.03(11) *
1123	1	132	71	0.758	0.777(08)	17.6	8.8	26.9	46.5	12.40	12.39	11.55	-21.78(13) *
A3193													
430691	5	12	9	0.542	0.559(12)	19.3	5.5	18.8	21.2	14.82	14.69	14.37	-20.70(07)
430695	5	6	144	0.447	0.461(27)	20.0	5.2	16.2	16.5	15.38	15.19	14.97	-20.11(07)
430697	3	12	158	0.658	0.688(07)	17.4	3.9	14.5	22.5	13.79	13.77	13.39	-21.69(06)
430698	5	14	57	0.689	0.722(09)	19.1	3.7	12.3	14.0	16.15	16.04	15.67	-19.41(07)
23113	5:	24	39	0.209	0.217(52)	18.9	3.7	11.3	15.6	14.26	14.19	14.13	-20.95(04)
23130	2:	33	165	0.420	0.423(40)	21.7	19.3	52.3	31.8	13.95	13.52	13.01	-22.07(12) *
23136	2:	36	45	0.293	0.300(25)	18.6	5.9	18.2	26.8	13.02	12.97	12.56	-22.51(06) *
A3381													
460069	2	6	17	0.639	0.671(09)	19.1	4.6	13.4	20.2	14.36	14.31	13.73	-21.58(07) *
460070	2	6	108	0.631	0.671(12)	18.8	3.5	10.2	15.0	15.20	15.15	14.43	-20.88(09)
460071	2B	4	127	0.524	0.539(35)	19.8	7.4	20.7	25.2	13.99	13.89	13.28	-22.03(09) *
460077	4:	8	180	0.420	0.439(31)	18.4	4.5	14.4	21.0	13.84	13.78	13.61	-21.18(04)
24895	4	23	149	0.641	0.672(15)	18.7	5.7	16.6	24.3	14.20	14.14	13.82	-21.49(06) *
A2295b													
270368	5	20	135	0.495	0.534(54)	19.4	3.3	10.1	12.2	15.60	15.51	15.14	-21.21(08)
270370	5	18	79	0.806	0.863(07)	20.0	4.2	13.2	13.8	17.02	16.85	16.00	-20.35(13) *
280128	4	18	100	0.667	0.732(17)	18.8	2.8	8.8	12.3	15.85	15.80	15.31	-21.04(10) *
280130	0	22	96	0.406	0.420(56)	20.7	7.6	16.9	19.7	14.29	14.15	13.60	-22.75(07) *
280134	4	28	16	0.728	0.786(08)	18.8	3.6	10.8	15.5	15.48	15.43	14.80	-21.18(12) *
A2295													
270373	3	13	53	0.440	0.482(28)	19.6	2.7	7.7	9.8	16.01	15.92	15.58	-21.37(06)
270375	4:	11	63	0.175	0.185(20)	19.4	3.9	10.2	14.6	14.40	14.32	14.20	-22.75(04) *

TABLE 3. Galaxy Photometric Parameters, by Cluster

Names	T	θ '	PA °	ϵ	ϵ_{cor}	$\mu(0)$	R_d "	R_{opt} "	$R_{23.5}$ "	$m_{23.5}$	m_∞	m_{cor}	M_{cor}
(1)	(2)	(3)	(4)	(5)	(6)	(7)	(8)	(9)	(10)	(11)	(12)	(13)	(14)
A2806													
20391	1	52	95	0.681	0.698(12)	17.9	7.7	27.8	39.5	12.72	12.69	12.10	-22.39(07) *
400697	5	60	72	0.804	0.823(13)	19.4	8.4	23.9	32.2	14.55	14.49	13.80	-21.15(11)
400698	3	37	0	0.602	0.637(15)	17.2	3.0	11.5	17.5	14.28	14.26	13.81	-20.68(07) *
400703	5	44	18	0.359	0.367(26)	19.7	7.2	21.4	25.0	13.94	13.81	13.63	-20.86(05) *
400704	5	42	143	0.421	0.441(24)	18.6	3.5	12.1	15.7	14.78	14.69	14.48	-20.01(05)
400706	5	12	74	0.755	0.776(19)	20.1	7.5	20.1	23.6	15.26	15.13	14.59	-19.90(10)
400713	5	8	44	0.561	0.582(16)	19.1	4.8	15.2	19.9	14.65	14.58	14.27	-20.23(06) *
20487	3:	57	5	0.635	0.647(10)	18.5	10.2	40.0	52.2	12.69	12.63	12.31	-22.18(06)
400727	5	35	141	0.717	0.744(08)	19.4	6.4	18.8	24.2	14.91	14.83	14.34	-20.15(09)
20512	1:	62	91	0.691	0.713(25)	18.1	6.3	25.9	36.8	13.16	13.14	12.52	-21.97(12)
20587	2	95	158	0.717	0.738(16)	19.0	8.7	26.2	36.0	13.44	13.38	12.71	-21.75(12)
A114													
400421	3	40	120	0.686	0.710(25)	19.0	5.8	17.6	23.6	14.32	14.26	13.85	-22.47(11)
400672	5	36	62	0.652	0.690(21)	19.4	3.4	10.2	12.8	16.01	15.92	15.45	-20.89(08) *
400673	5	33	104	0.588	0.638(07)	18.5	2.2	7.4	10.3	15.84	15.80	15.38	-20.87(07)
400674	5	32	143	0.800	0.836(14)	20.7	4.7	13.5	12.2	17.49	17.24	16.70	-19.54(11)
400443	1	21	48	0.341	0.366(89)	17.5	2.3	8.4	12.8	14.33	14.30	13.84	-22.33(07) *
400453	4	13	140	0.561	0.594(22)	18.1	2.7	10.7	13.6	14.75	14.70	14.42	-21.75(05) *
400686	3:	10	103	0.628	0.675(16)	18.9	2.8	8.5	11.9	15.73	15.66	15.29	-20.88(06)
400466	2	13	58	0.567	0.597(16)	18.7	3.9	11.7	17.2	14.63	14.58	14.03	-22.14(07)
400688	4:	5	112	0.616	0.632(07)	19.8	6.3	17.3	21.3	14.82	14.71	14.41	-21.76(06)
A119													
400611	2	29	8	0.653	0.674(20)	19.3	6.8	18.6	26.6	13.99	13.93	13.30	-22.00(07)
400619	3	21	9	0.690	0.713(17)	19.0	6.7	18.5	27.4	14.12	14.07	13.60	-21.98(10) *
400600	3	4	102	0.641	0.673(15)	18.1	4.3	12.9	21.1	14.09	14.06	13.62	-21.95(06) *
400641	3:	21	130	0.512	0.542(53)	18.5	3.9	12.8	18.2	14.35	14.30	13.97	-21.61(06) *
400653	6	26	91	0.749	0.794(10)	19.3	4.0	11.9	15.3	16.09	16.02	15.35	-20.23(10)
400658	5	53	44	0.579	0.604(22)	20.2	4.3	11.8	14.8	15.48	15.37	15.10	-21.66(05) *
A194													
784	3:	173	30	0.507	0.522(12)	18.9	7.1	22.6	29.3	13.43	13.37	12.95	-20.36(06) *
830	5	118	120	0.185	0.185(15)	20.5	13.5	52.4	37.1	13.38	13.09	12.98	-20.78(08) *
847	5	127	67	0.878	0.893(13)	20.1	14.6	41.8	46.0	14.72	14.57	13.56	-19.89(15)

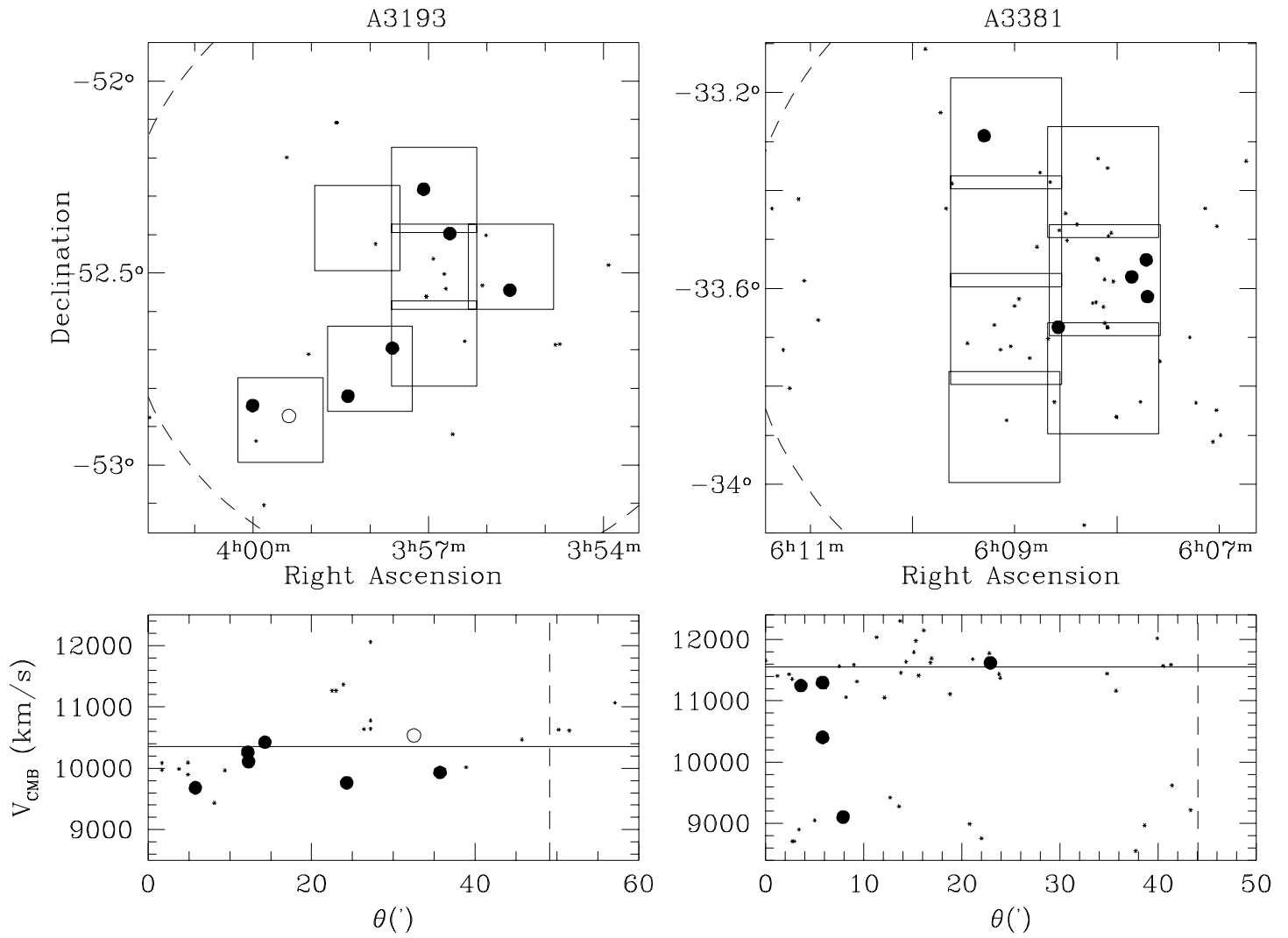


fig. 4

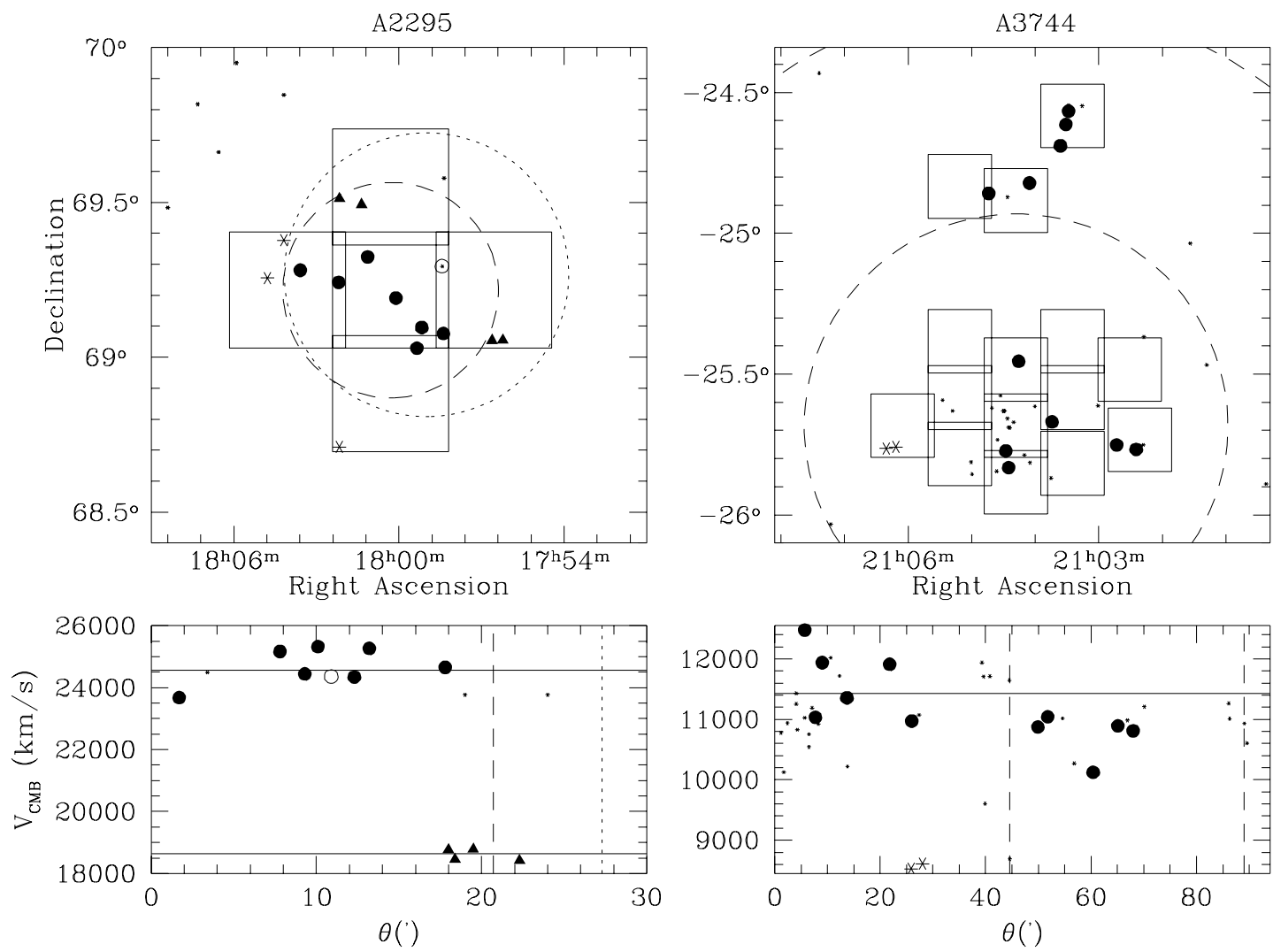


fig. 5

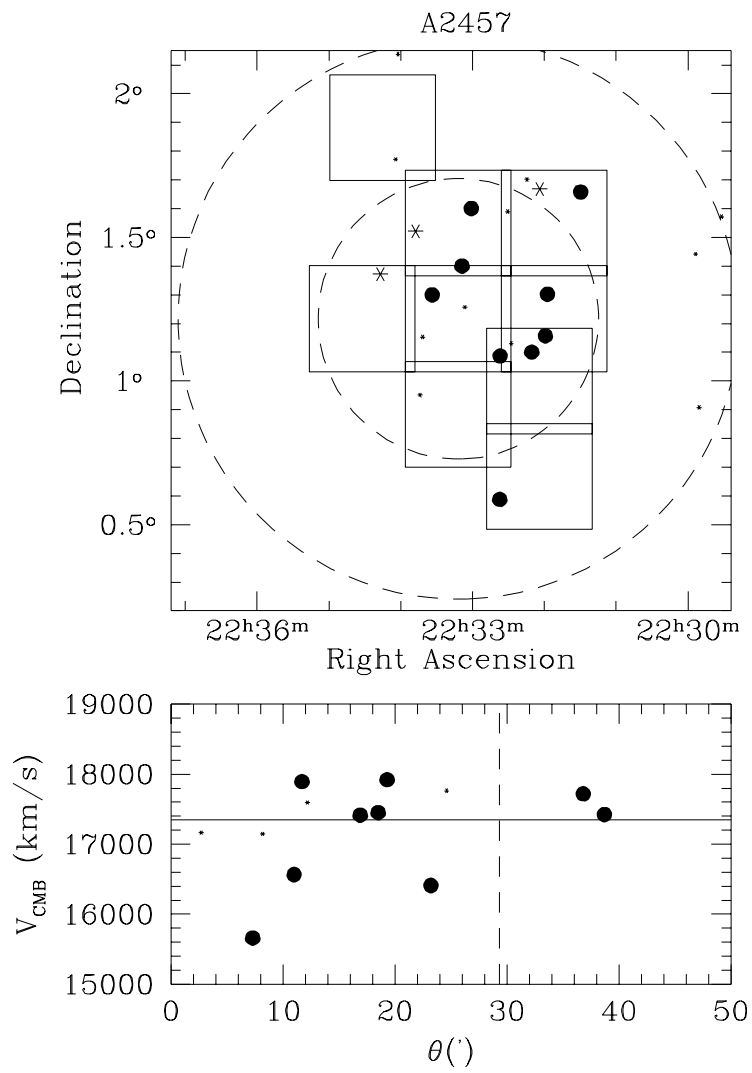
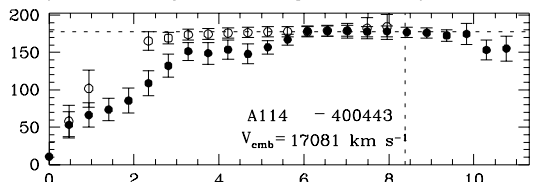
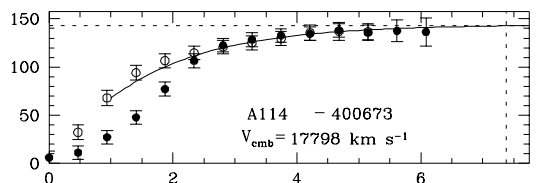
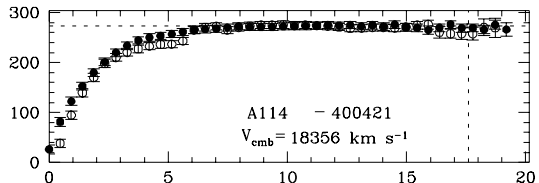
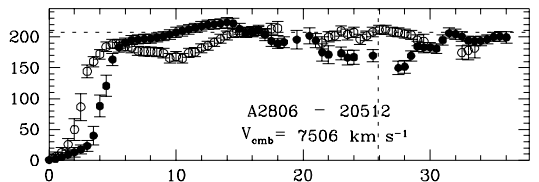
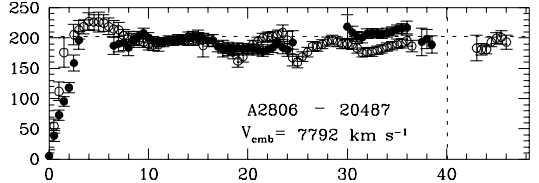
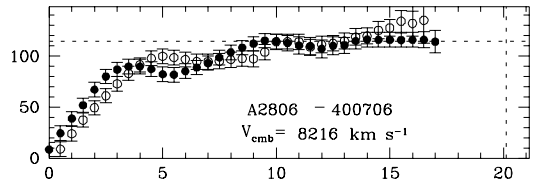
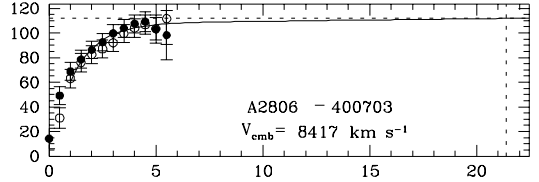
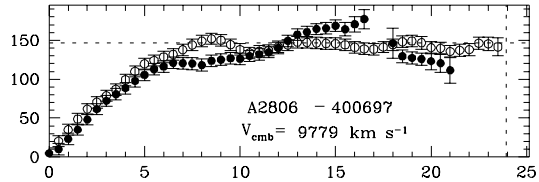
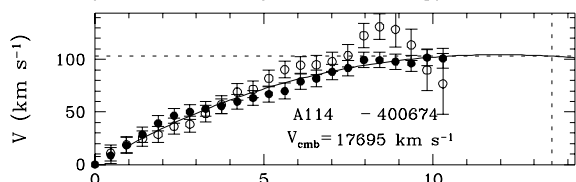
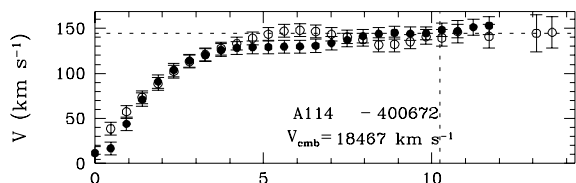
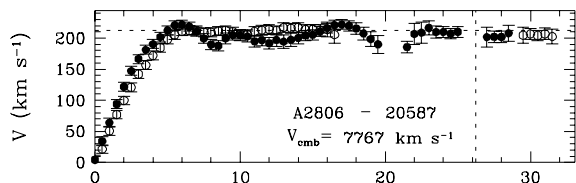
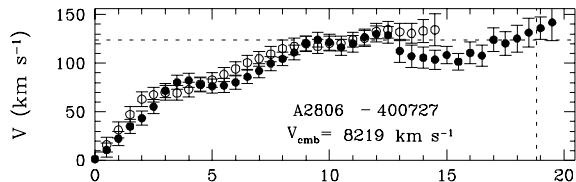
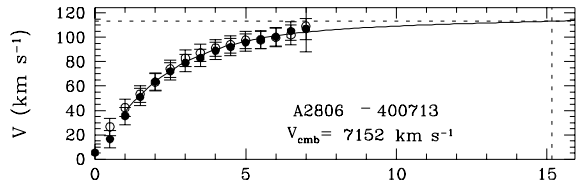
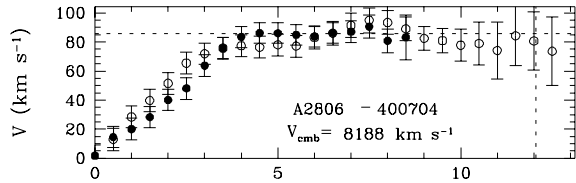
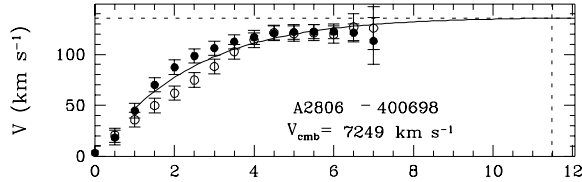
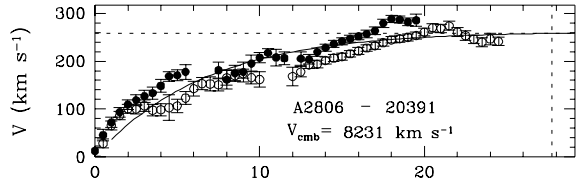


fig. 6



Radius (arcseconds)

Radius (arcseconds)

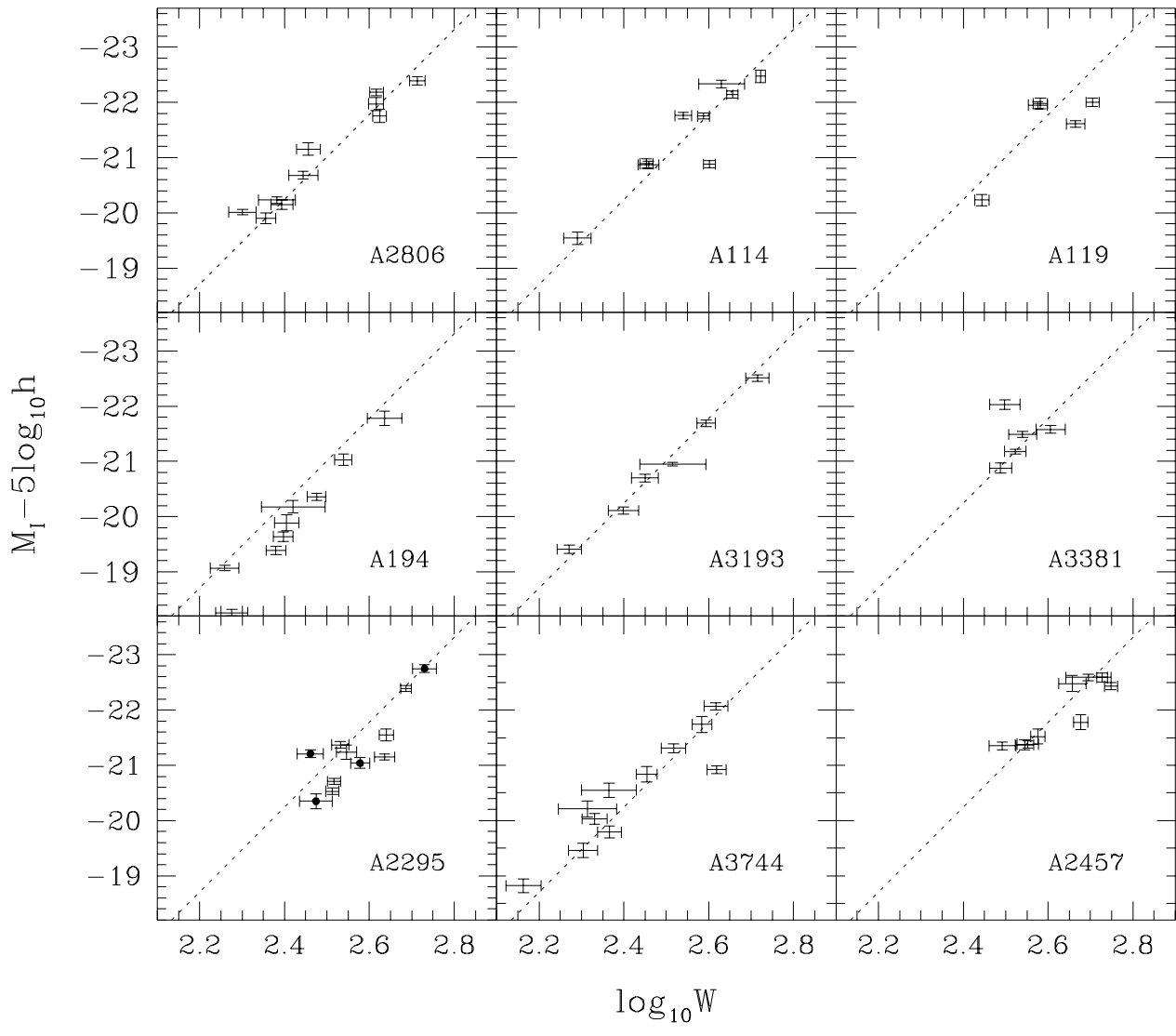


fig. 9